A precipiton method to calculate river hydrodynamics, with applications to flood prediction, landscape evolution models, and braiding instabilities

Philippe Davy, Thomas Croissant, Dimitri Lague

AGU PUBLICATIONS

JGR

Journal of Geophysical Research: Earth Surface

RESEARCH ARTICLE
10.1002/2016JF004156

Key Points:
- A particle-based, numerical approach is presented for rapidly solving the shallow water equations
- The method can solve both hydrodynamics and erosion and sediment transport equations
- The method is successful in creating a large variety of channel forms from straight to braided channels

Supporting Information:
- Supporting Information S1

Correspondence to:
P. Davy,
philippe.davy@univ-rennes1.fr

Citation:
Davy, P., T. Croissant, and D. Lague (2017), A precipiton method to calculate river hydrodynamics, with applications to flood prediction, landscape evolution models, and braiding instabilities, *J. Geophys. Res. Earth Surf.*, *122*, doi:10.1002/2016JF004156.

Received 25 NOV 2016
Accepted 11 JUL 2017
Accepted article online 18 JUL 2017

A precipiton method to calculate river hydrodynamics, with applications to flood prediction, landscape evolution models, and braiding instabilities

Philippe Davy[1], **Thomas Croissant**[1], **and Dimitri Lague**[1]

[1]Géosciences Rennes, OSUR, CNRS, Rennes, France

Abstract The "precipiton" method is a particle-based approach that consists of routing elementary water volumes on top of topography with erosive and depositional actions. Here we present an original way to calculate both river depth and velocity from a method that remains embedded in the precipiton framework. The method solves the governing equations for water depth, where the water depth is increased by a constant quantity at each precipiton passage and decreased by a value based on a flow resistance equation. The precipitons are then routed downstream on top of the resulting water surface. The method is applicable even if the precipitons are routed one by one (i.e., independent of each other), which makes it simple to implement and computationally fast. Compared to grid-based methods, this particle method is not subject to the classic drying-wetting issue, and allows for a straightforward implementation of sediment transfer functions between the river bed and running water. We have applied the method to different cases (channel flow, flow over topographic barriers, and flood prediction on high-resolution lidar topography). In all cases, the method is capable of solving the shallow water equations, neglecting inertia. When coupled with erosion and sediment transport equations, the model is able to reproduce both straight and braided patterns with geometries independent of grid size. Application of the model in the context of multithread rivers gives new insight into the development of braiding instability.

Plain Language Summary The "precipiton" method is a numerical method that consists in routing elementary water volumes on top of topography with erosive and deposition actions. Here we present an original way to calculate both river depth and velocity. The method consists in solving water depth from a differential equation, where the water depth is increased by a constant quantity at each precipiton passage and decreased by a value based on a flow resistance equation. The precipitons are then routed downstream on top of the resulting water surface. The method is applicable even if the precipitons are routed one by one, i.e., independently of each other, which makes it simple to implement and quite fast. Compared to grid-based methods, this particle method is versatile, fast, and allows for a straightforward implementation of sediment transfer functions between river bed and running water. We have applied the method to different cases (channel flow, flow over topographic bumps, or real cases with high-resolution lidar topography). In all cases, the method does very well in predicting the distribution of flood on landscapes. When coupled with erosion and sediment transport equations, the model is able to reproduce both straight and braided river patterns.

1. Introduction and State of the Art

The precipiton method is a particle-based approach, which mimics the role of precipitation (precipiton = elementary rainfall volume) on shaping topography [*Chase*, 1992; *Crave and Davy*, 2001; *Davy and Crave*, 2000; *Davy and Lague*, 2009; *De Boer*, 2001; *Favis-Mortlock*, 1998]. Together with cellular methods [*Coulthard and Van De Wiel*, 2006; *Fonstad*, 2006; *Murray and Paola*, 1994; *Nicholas*, 2005; *Thomas and Nicholas*, 2002], they have been popular for mimicking self-organized emerging properties of geomorphological systems, from high-resolution braided patterns to drainage network organization. Such high-resolution, high-frequency, fluvial geomorphic patterns and dynamics are beyond the scope of simple landscape evolution models, whose hydrodynamic description is much too rudimentary (see the state-of-the-art review by *Tucker and Hancock* [2010, and references therein]). Similarly, such conditions are rarely modeled over large spatial and temporal scales with sophisticated computational fluid dynamic models because of computational time, although recent progress is worth noting [*Jang and Shimizu*, 2005; *Nicholas et al.*, 2013; *Schuurman et al.*, 2013; *Wang et al.*, 2010].

Solving hydrodynamics constitutes a major difficulty for cellular automata and precipiton methods, and for some models a clear weakness that casts doubt on the relevance of results. The dependency of channel

geometry on grid size that was observed in the seminal model of *Murray and Paola* [1994], as well as in subsequent work [e.g., *Doeschl-Wilson and Ashmore*, 2005; *Nicholas and Quine*, 2007; *Ziliani et al*., 2013], emphasizes the limit of these reduced complexity models to obtain a realistic description of channel width dynamics. This issue reflects that the classic kinematic wave assumption used in these models neglects the water pressure depth gradient, although this force is critical to enable water to spread laterally over submerged banks, and for the channel to maintain a nonvanishing width (i.e., larger than the grid pixel) [e.g., *Coulthard et al*., 2013; *Izumi and Parker*, 1995; *Tucker and Hancock*, 2010]. Without this pressure gradient term, landscape evolution models are unable to predict channel width from erosion dynamics; they must specify it as an external relationship and basically consider channels to be 1-D "wires" surrounded by 3-D hillslopes. As this external relationship imposes a fixed relationship between channel width and mean discharge, these models cannot capture, for instance, the tendency for alluvial channel width to vary with sediment supply and/or incision rates [e.g., *Duvall et al*., 2004; *Lague*, 2010; *Lague*, 2014; *Lave and Avouac*, 2001; *Simon and Thorne*, 1996; *Whittaker et al*., 2007].

The concept of precipitons was originally introduced by *Chase* [1992] as a discrete representation of water volumes that are stochastically generated by rainfall, which then run over and erode topographic surfaces [*Chase*, 1992; *Crave and Davy*, 2001; *Davy and Crave*, 2000]. It is a Lagrangian method (equations are written in the fluid reference frame) that offers substantial advantages compared to the classic Eulerian methods:

1. Since particles are elementary flow elements, the largest density of particles is naturally encountered in large flows. Wetting (where flow spreads over dry areas) or drying (where flow no longer takes place) of the landscape is thus inherently solved by the displacement of precipitons, while it may remain a difficulty for Eulerian methods (see the discussion in *Bradford and Sanders* [2002] and in *Jang and Shimizu* [2005]).
2. The coupling between hydrodynamics and erosion/transport/deposition is straightforward since particles are flow elements eroding topography and transporting sediments, whereas implementation of these processes raises difficulties in classic numerical schemes for managing time scales of both flow depth and bed deformation [*Cao*, 2007].
3. The boundary conditions are easily managed: particles are introduced to each grid cell at a rate corresponding to the inflow, which can be either a rainfall rate or an upstream river discharge. The outlets are predefined; they are stop conditions for the particle walks.
4. Implementing nonlocal transfer, which results from sediment transfers between bed topography and running water over a wide range of spatial scales [*Foufoula-Georgiou et al*., 2010; *Stark et al*., 2009], is straightforward since erosion and deposition are different processes that occur during the precipiton path (see *Davy and Lague* [2009] and the concept of sediment transfer length, which is a way to model nonlocal transfers).

Up to now, the main drawback of the precipiton method is its very crude approximation of river hydrodynamics since the original method assumes that precipitons move down the steepest topographic slope independent of hydraulic gradients.

In this paper, we resolve this limitation by calculating both river depth and velocity from a method embedded in the precipiton framework, thus maintaining its computing efficiency. To our knowledge, this approach is the first attempt to solve the shallow water equations with precipiton methods in landscape evolution models. There are other particle-based methods available for solving hydrodynamics, such as smooth particle hydrodynamics [*Lee and Han*, 2010; *Solenthaler et al*., 2011], or particle-in-cell approaches [*Brackbill et al*., 1988; *Tetzlaff and Harbaugh*, 1989] that share most of the above-cited advantages. However, managing boundaries in more complex in these approaches [*Li and Liu*, 2002; *Liu and Liu*, 2003] and, unlike the precipiton method, they require calculating the interactions between particles, which is more computationally expensive.

The paper is organized as follows: first, the basic hydraulic equations and their implementation in the framework of precipitons are presented. Second we verify performance for several different cases using both idealized and natural topography, examining (i) flood propagation in an inclined rectangular channel, (ii) flow over a topographic barrier to evaluate the ability of the model to deal with lakes and dams, and (iii) flood inundation in a natural river valley using high-resolution LiDAR topography. In this step, we also compare our method to the storage cell inundation model *Lisflood-FP* [*Bates et al*., 2010] that has been recently coupled with the cellular automata model *CAESAR* to fully solve the shallow water equations in landscape evolution models [*Coulthard et al*., 2013]. Lastly, we apply the new model to a high-resolution topography obtained with lidar. Lastly, we show how the model can be coupled with

erosion and deposition rules to model channel morphodynamics, and we discuss application of our approach for modeling landscape evolution. We present two types of morphodynamic experiments: (i) the incision of a straight channel that demonstrates the robustness of the numerical method and the role of lateral erosion and (ii) the development of multithread braiding patterns that demonstrates the ability of the model to simulate different hydromorphic regimes, providing new insights on braiding instability (a generic term which indicates the occurrence of a dynamic braided morphology).

2. A Particle Method for Solving Hydrodynamics

The precipiton method routes elementary water volumes (precipitons) that interact with topography. The precipitons move according to hydrodynamic equations, and modify topography by erosion and deposition laws dependent on both hydraulic conditions (i.e., shear stress, discharge calculated at each grid cell from the frequency of precipiton passages over the cell, or slope) and sediment volume carried by the precipiton. A more complete description of the method, and of the €ros code, is available in *Crave and Davy* [2001], as well as in *Davy and Crave* [2000] and *Davy and Lague* [2009]. An intrinsic geometric aspect of the precipiton method is that particles move independently on a fixed rectangular grid, where the elementary displacements are restricted to the eight nearby neighbors (D8 method [*Tarboton*, 1997]), as in cellular automaton methods. The hydraulic flux is defined statistically as the average over a large number of particles, whose direction is defined from a probabilistic distribution function that depends on local slope. It is thus not restricted to one of the eight neighbor directions.

In the initial version, hydrodynamics merely consists of moving precipitons downward in the direction of topographic slope. We show in the next paragraphs how the 2-D shallow water equations (without the inertia terms) can be implemented in the precipiton framework.

2.1. Basic Equations of Hydrodynamics

The 2-D shallow water equations are a widely used approximation of the 3-D Navier-Stokes equation for applications such as the evaluation of flooded areas, erosion and sediment transport predictions, and landscape evolution models (see review in *Horritt and Bates* [2002]). The basic equations are the conservation of mass and the conservation of momentum equations integrated over the flow depth, where the basic forces are gravity and friction drag. The water balance is written (with Einstein notation) as

$$\frac{\partial h}{\partial t} + \partial_i q_i = 0 \tag{1}$$

where h is the water depth, t is the time, and q_i is the flow discharge vector, where $q_i = hu_i$ with u_i as the mean flow velocity vector. The momentum equation is

$$\rho h\left(\frac{\partial u_i}{\partial t} + u_j\frac{\partial u_i}{\partial x_j}\right) = \rho g h\left(\frac{\partial h}{dx_i} + \frac{\partial Z}{dx_i}\right) - \tau_i \tag{2}$$

where Z is the bed elevation, τ_i is the shear stress acting on the river bed, ρ is the water density, x_i and x_j are the horizontal coordinates, u_i and u_j are the horizontal velocity coordinates, and g is the gravitational constant. The shear stress τ_i is assumed to be maximum along the flow path and zero perpendicular to flow.

The left-side terms represent inertia. The first term is the local acceleration ($\rho h \frac{\partial u_i}{\partial t}$), which vanishes at steady state, but has been found to capture a large part of the nonstationary flooding characteristics [*de Almeida and Bates*, 2013]. The second left-side term represents the convective acceleration; it is important with large spatial variations of discharge intensity or direction, and often negligible where the flow varies gradually.

The right-side terms represent both driving (gravity) and resisting forces. The first, ($\rho g h \frac{\partial h}{dx_i}$), is the fluid pressure term. The second is the resistance of the channel bed and banks to flow, which is collinear with the flow velocity such as

$$\tau_i = K(h)|u|u_i \tag{3}$$

where $|u|$ is the velocity modulus and $K(h)$ is a function which is found to be slightly dependent on h in experiments (*Manning* [1891] model) or modeled as a constant (Darcy-Weisbach). K is dependent on the rugosity of the river bed. Equation (3) implicitly assumes that the basal friction on the river bed is much larger than any of the other frictional terms, such as lateral bank friction and viscous drag in the water column.

If we assume that the inertial terms are negligible, the momentum equation (2) provides two critical pieces of information: the flow velocity u_i is parallel to the water surface slope s_i, and both quantities are related by the following relationship (also called the "friction" equation in the following):

$$u_i = Ch^{\alpha}\frac{s_i}{\sqrt{s}}H(s_i) \tag{4}$$

where α is an exponent equal to $\frac{1}{2}$ for the Darcy-Weisbach model and $\frac{2}{3}$ for the Manning equation; C is a constant defined by $C = \frac{\rho g h^{\frac{1}{2}-\alpha}}{K(h)^2}$; s_i is the hydraulic slope in the direction i; H is the Heaviside function (1 if positive, 0 if negative), which indicates that no displacement is expected with negative (i.e., upward) slope; and s is the steepest slope (largest positive slope value).

The minimum requirement to take into account the pressure gradients is to consider s_i in equation (4) as the slope of the water surface rather than of topography. This implies that one must solve equations (1) and (2) (or equation (4)) in 2-D to derive both water depth h and velocity u_i as is classically done in flood inundation models (see review in *Horritt and Bates* [2002]). The computational cost of doing so is prohibitive for landscape evolution models, although significant improvements have been obtained in modeling the long-term evolution of braided and meandering patterns [*Jang and Shimizu*, 2005; *Nicholas et al*., 2013; *Ruther and Olsen*, 2007]. Recent advances with cellular automata techniques are also worth noting [*Coulthard et al*., 2013], which couple the erosion/deposition code *CAESAR* with *Lisflood-FP* [*Bates and De Roo*, 2000].

2.2. A Stochastic Particle-Based Method for Solving Hydrodynamics

We propose to improve hydrodynamics by solving equations (1) and (4) (i.e., by neglecting the inertia terms in equation (2)). The basic requirement to take into account hydrodynamics is that the particle velocity (and thus direction) is defined according to equation (4), which routes the precipiton based upon the water surface slope rather than on topography. A stochastic algorithm is implemented where the particle direction is chosen probabilistically as a function of velocity and of water surface slope:

$$P_i \sim u_i \sim \sqrt{H(s_i)s_i} \tag{5}$$

where P_i is the probability for the particle to follow the direction i. The probability term ensures that all possible directions defined in equation (4) are actually sampled probabilistically, which minimized the occurrence of long-range preferential flow along the eight primary orientations, although each precipiton runs along discrete directions (D8) of the grid. Equation (5) represents the stochastic equivalent of the directional component of the friction equation (4).

The stochastic walk results in a series of precipitons that pass through each grid cell at a frequency proportional to the local discharge [*Crave and Davy*, 2001]. The inflow of precipiton in a cell defines the total water discharge Q:

$$Q = \Sigma_p V_{in}^p \delta(t^p) \tag{6}$$

p numbers the list of precipitons that pass through the cell at time t^p. V_{in}^p is the volume of water carried by the precipiton p when entering the cell, and δ is the Dirac delta function. The integral of Q over time is the total volume of water entering the cell. Because of the stochasticity introduced in the precipiton creation and routing (equation (5)), the passage of particles through a cell is a Poisson process, where the arrival time of a particle t_p is independent of the others (Markov hypothesis). Thus, the time interval between successive precipitons ($\Delta t^p = t^p - t^{p-1}$) is exponentially distributed with a characteristic time equal to the ratio V/Q, where V is the average volume of a precipiton [*Crave and Davy*, 2001].

The basic idea of the method is to calculate the water depth h resulting from a stochastic differential equation that expresses a water mass balance equation for each grid cell:

$$A\frac{\mathrm{d}h}{\mathrm{d}t} = -\phi(h,s) + Q = -\phi(h,s) + \Sigma_p \Sigma_p V_{in}^p \delta(t^p) \tag{7}$$

where A is the cell area. In equation (7), the cell is filled up by precipitons (last hand-right term), which run out at a rate given by the flow rate function $\phi(h,s)$ (first right-hand term) whose direction is given by the

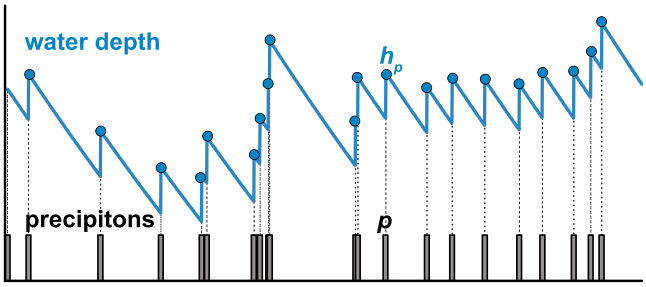

Figure 1. Schematic graph showing the evolution of (top) water depth and (bottom) precipiton arrival with time in a cell. The water depth increases abruptly at each precipiton passage and then decreases gradually according to equation (10). The solid symbol indicates the series of water depth $\{h^p\}$ defined at each precipiton arrival.

precipiton displacement (equation (5)). The choice of the function ϕ is the key point of the method; we define it as the flow rate given by the friction equation (4), which is either the Manning or Darcy-Weisbach relationship:

$$\phi(h,s) = dw\ uh = dw\ C\sqrt{s}h^{\alpha+1} \quad (8)$$

where dw is the flow width equal to the cell area A divided by the channel length dl and s is the slope at time t. The way the flux ϕ leaks out of the cell with precipitons is explained in a next paragraph.

Since the inflow occurs at discrete times, equation (7) solves a first-order differential equation between two successive precipitons:

$$\frac{\mathrm{d}h}{\mathrm{d}t} = -\frac{\phi(h,s)}{A} \quad (9)$$

where the flow length dl is the grid cell dimension parallel to the flow direction. Because of the D8 directions, dl can be either the grid cell side size or the diagonal size, but the product length by width ($dl\,.\,dw$) is always equal to the cell area A. The equation becomes

$$\frac{\mathrm{d}h}{\mathrm{d}t} = -\frac{C}{dl}\sqrt{s}h^{\alpha+1} \quad (10)$$

This first-order differential equation indicates that the cell is emptying with an apparent time scale of $\frac{dl}{u(h,s)}$. It can be solved analytically if the slope s is assumed constant. Combined with equation (7), this gives the following expressions:

$$\text{if } t < t^p : h(t) = h^{p-1}\left(1 + \alpha\frac{C}{dl}\sqrt{s}\left(h^{p-1}\right)^{\alpha}\left(t - t^{p-1}\right)\right)^{-1/\alpha} \quad (11)$$

$$\text{for } t = t^p : h^p = h^{p-1}\left(1 + \alpha\frac{C}{dl}\sqrt{s}\left(h^{p-1}\right)^{\alpha}\left(t - t^{p-1}\right)\right)^{-\frac{1}{\alpha}} + \frac{V^p}{A} \quad (12)$$

where the series $\{h^p\}$ refers to the water depth at time t^p, just after the volume increase (i.e., the relative maxima observed in Figure 1, which shows an example of such evolution).

The series $\{h^p\}$ constitutes the solution of the stochastic equation (7). An example of a typical evolution is given in Figure 1. If the fluctuations are small enough, the average water depth $\overline{h} = \langle h^p \rangle$ is the value predicted by the friction equation (4): $q = \frac{Q}{dw} = C\sqrt{s}\overline{h}^{\alpha+1}$ (see the demonstration given in Appendix A for small fluctuations). The discrete arrivals of precipitons are implicit to the method and cause fluctuations that are not necessarily physically relevant (although Figure 1 is typical of natural systems with a rapid increase of discharge and water depth following rainfall, and then a slow decrease). The validity and accuracy of the method is then directly related to the fluctuation amplitude around the average, which increases with volume size V^p_{in} and thus time step, as for any numerical method. Thus, equation (12) constitutes the stochastic equivalent of the friction equation (4).

Equation (12) also defines the precipiton volume V^p_{out} when leaving out the cell. To maintain a global mass balance for water, it must be equal to the total volume of water lost by the cell since the latest precipiton $p-1$, just before being filled up by the precipiton P:

$$V^p_{\text{out}} = \int_{t^{p-1}}^{t^p} \phi(h,s)\,\mathrm{d}t = V^p_{\text{in}} + A\left(h^{p-1} - h^p\right) \quad (13)$$

V^p_{out} becomes the inflow precipiton volume for the next cell visited by the precipiton. Note that $V^p_{\text{out}} = V^p_{\text{in}}$ if $h^p = h^{p-1}$, which happens when the solution is stationary. Equation (13) is the actual equivalent of the mass balance equation (1).

The numerical simulations consist of a five-stage process (in bracket, we give the continuous equivalent):

1. ("*rainfall*" *inflow*) Precipitons are stochastically created according to an inflow map, which describes all the processes that contribute to flow on topography (rainfall, channel discharge, or groundwater seepage). The initial volume of precipiton is $V_o^p = Q.dt$, where Q is the local inflow or discharge and dt is the time increment between two successive precipitons "launched" on the grid, wherever they land on.
2. (*friction equation*) The friction equation results in several steps:
   - 2.1 Water depths are first calculated at the time $t = t^p$ from equation (12) for the current cell or equation (11) for neighbors, which are the approximate solutions of equation (7), valid for constant slope. The parameters of both equations (slope, direction) are those prevailing the last time cells were updated ($t = t^{p-1}$ for the current cell).
   - 2.2 Water surface slopes are calculated from the updated water depths.
   - 2.3 The parameters (slope, *dl*) of equations (11) and (12) are updated.
3. (*advection*) Precipitons are routed toward a neighboring cell according to equation (5). If the hydrodynamic model is coupled with erosion and sediment transport processes, this is done at this stage during the displacement of the precipiton.
4. (*mass balance equation*) The precipiton volume is updated by applying equation (13).
5. (*boundary conditions*) The precipiton path stops when it reaches grid points prescribed as "absorbing" boundary elements. Since the downward slope cannot be calculated for these points, the water depth must be fixed by a relationship, or calculated in the same manner as others by using a surrogate value of water slope: that of the upstream cell or the topographic slope. The latter is used in the presented simulations.

It is also possible to use a "stationary" variant of the preceding scheme, where the precipiton volume is not updated in stage 4.

4b. The precipiton keeps its initial volume all along its path. The transient stages are not described correctly, but the solution goes quickly to the stationary solution (h independent of t) since the precipiton "fills" all downstream points with a constant volume V_o^p. Since the stationary stage is defined as $V_{\text{out}}^p = V_{\text{in}}^p$, the solution is similar to the final stage of the full equation. With this variant, the water mass balance is not ensured for each precipiton, but is achieved on average. The stationary solution is much faster than the transient one (i.e., more than 10 times) because it reduces the water depth fluctuations inherent in this stochastic method, and thus allows for larger time steps.

Hereafter, we discuss a few important points of the model.

2.2.1. Why This Is a Stochastic Equation

The basic equations (5) and (7) contain stochastic terms both in the direction probability P_i and in the t^p series, with a Poisson distribution of interevent time lapses $t^p - t^{p-1}$ used in equations (11) and (12). The spatial derivatives that are intrinsic to the basic equations (1) and (2) are ensured by the variations of the precipiton paths. The speed of the method is largely due to the fact that precipitons are independent of each other, i.e., launched one by one. The relationships between adjacent cells are mainly provided by the time series t_p and h_p that are recorded for each cell of the grid.

2.2.2. Stability Criteria

We propose here an attempt to formalize a stability criterion for the method. The results will be checked with numerical examples in the following sections.

As shown in Figure 1, the method induces time fluctuations of the water surface, which in turn modifies the slope distribution s_i. If the fluctuations are larger than the general "expected" slope s, the precipiton walk will be considerably perturbed and the numerical solution will not converge to the expected one.

The water surface fluctuations have two sources: (1) the increase $\frac{\overline{V^p}}{\Delta x \Delta y}$ at each precipiton passage (see equations (11) and (12) and Figures 1 and 2) and (2) the fluctuations of the time series $\Delta t^p = t^p - t^{p-1}$. Both affect the considered cell but also for its neighbors, and thus contribute to modifying slopes s_i. To quantify these effects, we start from the linearized form of equation (12), valid for small values of $\Delta t^p = t^p - t^{p-1}$:

$$\Delta h^p = h^p - h^{p-1} \cong -\frac{C}{dl}\sqrt{s}\left(h^{p-1}\right)^{\alpha+1}\Delta t^p + \frac{V^p}{\Delta x.\Delta y} \tag{14}$$

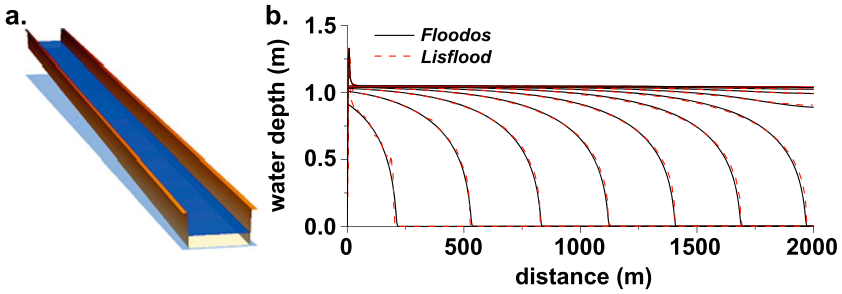

Figure 2. (a) Straight rectangular channel used to compute water depth. (b) Predicted water depth at different time steps for the two models. Predictions of Floodos are in good agreement with Lisflood-FP.

For stationary solutions, Δh^p is null on average ($\overline{\Delta h^p} = 0$), so the first and second right-hand terms of equation (14) are on average identical. Since V^p is constant, the fluctuations $\sigma_{\Delta h^p}$ of Δh^p are due both to the fluctuation of Δt^p, $\sigma_{\Delta t^p}$, and to the fluctuations σ_{h^p} of h^{p-1}. The series of precipiton arrival times in a cell is a Poisson process, which has two consequences for this calculation: the time lapse between two successive events is exponentially distributed, with $\sigma_{\Delta t^p} = \overline{\Delta t^p}$, and the fluctuations of Δt^p are much larger than of h^p if V^p is small enough (indeed, $\frac{\sigma_{h^p}}{\overline{h^p}} \ll \frac{\sigma_{\Delta t^p}}{\overline{\Delta t^p}} = 1$). The fluctuation of Δh^p is thus mostly due to $\sigma_{\Delta t^p}$ such as

$$\sigma_{\Delta h^p} = \frac{C}{\Delta x}\sqrt{\overline{sh^p}}^{\alpha+1}\sigma_{\Delta t^p} = \frac{C}{\Delta x}\sqrt{\overline{sh^p}}^{\alpha+1}\Delta t^p = \frac{V^p}{\Delta x.\Delta y} \tag{15}$$

This demonstrates that the accuracy in predicting water depth is directly proportional to the precipiton volume, which is confirmed by numerical simulations.

A stability condition for the numerical scheme is that the fluctuation of water surface does not affect significantly the downward routing of precipitons, in other words, that the amplitude of fluctuations must remain smaller than the variations due to water slope *s*:

$$\frac{\overline{V^p}}{\Delta x \cdot \Delta y} \ll s\Delta x \tag{16}$$

This prediction will be tested in the following simulations:

2.2.3. Can We Avoid Calculating the Transfer Time t_p?

To speed up simulations, we assume that, in any cell of the precipiton path, the difference in time between two successive precipitons, $\Delta t^p = t^p - t^{p-1}$ (see equations (7) and (12)), is well predicted by the average of the initial difference $\Delta t_o^p = t_o^p - t_o^{p-1}$, where t_o^p is the creation time of the precipiton *P*. This assumption is valid if the transfer time is short compared to the time between two successive precipitons or if the transfer time to a given cell is equivalent for all the precipitons. This is thus a reasonable assumption if a precipiton is an erosive rain event that occurs only a few times a year, as it was assumed in *Chase* [1992] and *Crave and Davy* [2001]. For hydrodynamic issues, such as flood prediction, this assumption is no longer valid, and a transfer time should be calculated for evaluating Δt^p. However, the method does not require to know precisely all Δt^p values in all cells, but only the average $\overline{\Delta t^p}$ over a certain time scale t_{avg}, which can be much longer than each Δt_p. It is easy to demonstrate that $\overline{\Delta t^p} \sim \overline{\Delta t_o^p}$ if the averaging time t_{avg} is longer than the transfer time of precipitons. Indeed, the total number of precipitons passing through the cell during t_{avg} will not be very different if we take account of the transfer time or not.

2.2.4. Lakes

"Lakes" are local minima of topography (and thus of the associated gravity field), where the definition of flow directions from particle motions poses a challenge [*Martz and Garbrecht*, 1998; *Turcotte et al.*, 2001]. Since the water surface $h(x, y)$ is expected to be flat on average in lakes, the precipiton displacement is mainly controlled by the "rugosity" of *h* (see section 2.2.2). This induces a diffusion-like displacement of precipitons, which achieve the lake filling. The tests that we present below demonstrate the ability of the precipiton method to efficiently resolve this issue with no significant additional computational time.

Table 1. Model Parameters for the Simulations Presented in Figures 2–9

	Width (pixel)	Length (pixel)	Wet Pixels (pixel)	Δx (m)	Inflow ($m^3\ s^{-1}$)	Slope	n ($s\ m^{-1/3}$)	CPU Time (min)	Figures
Rectangular channel	100	2,000	200,000	1	120	0.002	0.04	12.48	3b and 9
	50	1,000	50,000	2	120	0.002	0.04	2.1	2a, 3a, 3b, and 9
	25	500	12,500	4	120	0.002	0.04	0.57	3b and 9
Bump	20	250	50,000	0.1	0.02–0.2	0.001	0.04	-	4
Cruz lidar DEM (reach mode)	2,053	1,352	286,000	2.5	500	-	0.04	34	5c, 7a, 7c, and 9
	685	451	36,500	7.5	500	-	0.04	1.4	6 and 9
	229	151	4,190	22.5	500	-	0.04	0.05	7b, 7c, and 9
Cruz lidar DEM (catchment mode)	331	396	131,076	7.5	60	-	0.04	4	8

2.2.5. Numerical Implementation

The precipiton model has been implemented in C++ according to the description given in the previous paragraph. The code is called *Floodos* hereafter and is available under the GNU/GPL license.

3. Hydraulic Simulations and Comparison With Other Methods

All the simulations described below have been performed by considering a Manning relationship for flow resistance with a Manning coefficient of 0.04. The coefficients of equation (4) are thus $\alpha = \frac{2}{3}$ and $C = \frac{1}{n} = 25$.

3.1. Transient Experiments

The objective of the first test is to check the ability of *Floodos* to model the transient behavior of flood propagation. We assess the accuracy of the water depth prediction for a simple rectangular channel with constant upstream flow conditions (Figure 2a). The model parameters are given in the Table 1. Calculations have been performed in the nonstationary mode as described above, similar to a dam-break flood event, with no bank friction.

Predicted water depths were compared with *Lisflood-FP*, one of the most used numerical model in flood prediction [*Bates et al*., 2010; *Coulthard et al*., 2013] whose predictions have been benchmarked [*Bates et al*., 2010; *Hunter et al*., 2005]. We used the implementation of *Lisflood-FP* in *CAESAR:CAESAR–Lisflood* 1.6a [*Coulthard et al*., 2013].

Figure 2b shows a comparison of water depth as a function of distance for different time steps between *Lisflood-FP* and our model. *LisFlood-FP* uses the same concept of storage area as *Floodos* (i.e., water is stored in the grid and flows into and out of each cell) [*Bates et al*., 2010], but it solves equations from a finite difference discretization of time and space, while *Floodos* solves equations along the particle paths. *LisFlood-FP* also solves inertia terms of the shallow water equations, while *Floodos* does not solve them yet; these terms are negligible in the presented test.

Results show that *Floodos* perfectly matches the predictions of *Lisflood-FP* for each time step of the simulation, demonstrating the ability of our model to reproduce the transient behavior of flood propagation. Except for the first four lines close to the boundary, for which *Floodos* shows boundary effects, the difference between both models is about 0.5% on average.

3.2. Stationary Mode and Convergence Conditions

In this second test, we check the numerical conditions for which the stationary mode (point 4b in the code description; section 2.2) is stable. In the stationary mode, the precipiton keeps its initial volume all along its path (i.e., V^p = constant), entailing a faster filling of the water volume and thus a much shorter time to reach the stationary regime. To test the accuracy and the increased efficiency of our approach, we use the same parameters as in the previous case. Given the rectangular shape of the channel and the fact that only the basal friction is considered in this example (see the discussion after equation (3)), this experiment can be easily compared to a 1-D Manning analytical solution, although the calculation is actually performed in 2-D. Figure 3a shows the calculated water depth as a function of time, for different calculation time steps dt (and thus precipiton volume $V^p = Q\,.\,dt$, with Q as the inflow). The first stage of water depth increase corresponds to the infilling of the rectangular channel, whose

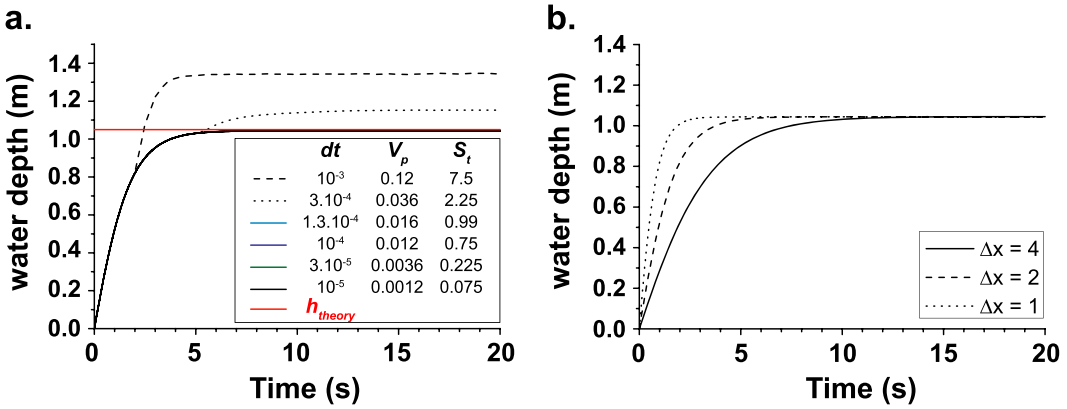

Figure 3. (a) Water depth evolution through time for different time steps *dt*, precipiton volumes V^p, and for a stability criterion S_t. Values are indicated in the framed box. (b) Water depth evolution through time for different grid cell resolutions for $S_t = 0.75$.

time scale depends on the grid size but not on the elementary precipiton volume V^p (see the discussion below). The number of precipitons required to reach stationary is thus inversely proportional to V^p.

Although each run converges at some point to a stationary solution, the obtained value is correct only for small precipiton volume V^p (full lines in Figure 3a). The stability criterion corresponds to a critical precipiton volume V_c^p about equals to 2×10^{-2} m^3. We verify the conjecture formulated in the previous paragraph that the precipiton volume should remain smaller than water height difference between adjacent cells along stream (equation (16)). We found here that, given the water surface slope s_o, the ratio $S_t = \frac{V^p}{s_o \Delta x^2 \Delta y}$ must remain smaller than 0.75.

The effect of the grid size, Δx, on the water depth calculation is shown in the Figure 3b. In order to compare results from the different tests, the time step value *dt* (or precipiton volume V^p) was chosen as the largest that respects the stability criteria $S_t = 0.75$. The time to stationary solution increases with Δx. This result is the direct consequence of the method. Indeed, each precipiton fills the downstream grid cells by a volume $V^p = Qdt$. Thus, the total amount of water brought by precipiton in the system is $V^p \frac{L_x}{\Delta x}$, and the number of precipiton to reach a given water depth h_c is the ratio between the total volume, and the volume brought by precipiton $n^p = \frac{h_c L_y}{V^p} \frac{\Delta x}{}$. Replacing V^p by its value given by the stability criterion leads to $n^p = \frac{h_c L_y}{S_t s_o \Delta x \Delta y} = \frac{h_c}{S_t s_o L_x} N_t$, where N_t is the number of grid cells. This result shows that the number of precipiton necessary to bring the required amount of water basically increases as the number of grid cells for a given stability criterion S_t. As observed in Figure 3b, the corresponding time $t = \frac{n^p V^p}{Q_o} = \frac{h_c L_y}{Q_o} \frac{\Delta x}{}$ increases linearly with Δx.

The dependency of the computational time with resolution will be discussed in section 1.

3.3. Dam

This test was designed to evaluate the effectiveness of the method to fill up lakes and dams. The initial topography is a straight channel with a hump in the middle that acts as barrier for the precipiton walk toward the downstream boundary (Figure 4a). Two discharges were tested (Figure 4b): $Q = 0.2$ (top), for which the water depth *h* without hump is larger than the hump height, and $Q = 0.02$ (bottom), for which *h* without hump is smaller. The test characteristics are given in the Table 1; it was performed in the stationary mode.

Precipitons successfully fill the volume upstream of the hump, forming a lake, with the average hydraulic slope and depth dependent on both the hump height and inflow. The lake eventually overtops the dam to flow downstream. With the stationary mode, one precipiton can fill up the volume upstream of the hump, since it brings its water volume to each cell it goes through. The water thus continues to be routed as long as it runs above the hump and can reach the downstream boundary. The water depth downstream of the hump is consistent with the expected theoretical value, calculated by assuming that the water slope is similar to topographic slope (Figure 4b). Upstream of the hump, the water depth is slightly larger than the top of the hump with a water slope slightly lower than the topographic slope. As expected, smaller discharges have less steep slopes. We check that the friction equation (4)) is verified for each section of the canal.

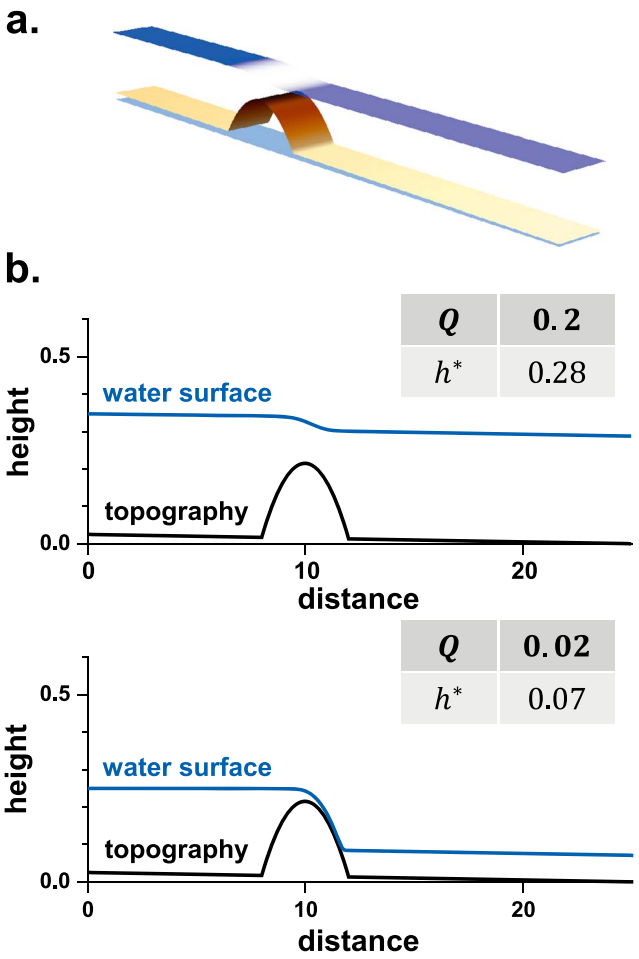

Figure 4. (a) Straight channel with a bump of maximum height 0.2 in the middle. (b) Water depth for both discharges (top) 0.2 and (bottom) 0.02. h^* is the stationary river depth without bump calculated for the discharge Q and channel geometry according to equation (4).

The hump problem addresses the subcritical versus supercritical nature of the flow, which was initially posed for frictionless flow. Since the momentum terms are neglected in this version of the code (equation (3) compared to equation (2)), the flow is subcritical and affected by downstream controls. However, precipitons are moving on top of the water surface, which precludes the formation of local minima in the water surface, as would occur in the theoretical solution of the hump problem for some subcritical conditions, and flat-water surfaces form instead.

3.4. Real-Case Applications With Lidar DEM

A potential application of the model is the prediction of flood levels from high-resolution digital elevation models (DEMs) that are now regularly acquired from airborne lidar. The test was applied on the Cruz River near Cruz Rock (CA, USA), whose lidar DEM acquired in the project *PG&E Diablo Canyon Power Plant* at an original resolution of 1 m is available on the web platform OpenTopography (http://www.opentopography.org/). The DEM has been degraded to 2.5 m for our study (Figure 5a). The modeling challenge is to deal with a complex floodplain containing geomorphological features such as multiple channels, terraces, bars, and a partial dam at the outlet (an actual bridge treated as a dam after the rasterization of the lidar 3-D data). The high-resolution DEM contains pits (i.e., local topographic minima), especially in the floodplain, which like lakes are a challenge for traditional flow routing models [*Zhu et al*., 2013]. To evaluate the robustness of our method to pits, we use the topography as is, i.e., without erasing pits with a depression filling algorithm.

We use the model under the stationary mode with simplified boundary conditions consisting of water input localized on pixels at the upstream river boundary. With these conditions, the water depth is computed only on pixels where the river actually flows. The river discharge has been fixed at ~500 $m^3\ s^{-1}$ to ensure an overbank flow in the floodplain.

Since the friction equation (4) is not an a priori constraint, but rather emerges from the model rules, we check if it is valid at every point by comparing the water depth derived from the simulation with the one expected from equation (4) given q and s. Figure 5c shows that there the friction equation is verified with a very good accuracy for all pixels (average standard deviation of 0.004 m between calculated and predicted values).

The model also manages to calculate flow around the artificial dam (Figures 5a and, 5b) with local holes in the river bed (see for instance the downstream part of the bridge/dam in Figure 5c). This demonstrates its ability to deal with high-resolution DEMs, even with high-frequency variations in topography, whether it is real or not.

Note that, in the stationary regime, *Floodos* can calculate the flood extent for a particular discharge (Figure 6), but the flood spreading from inlet must be calculated with the nonstationary version.

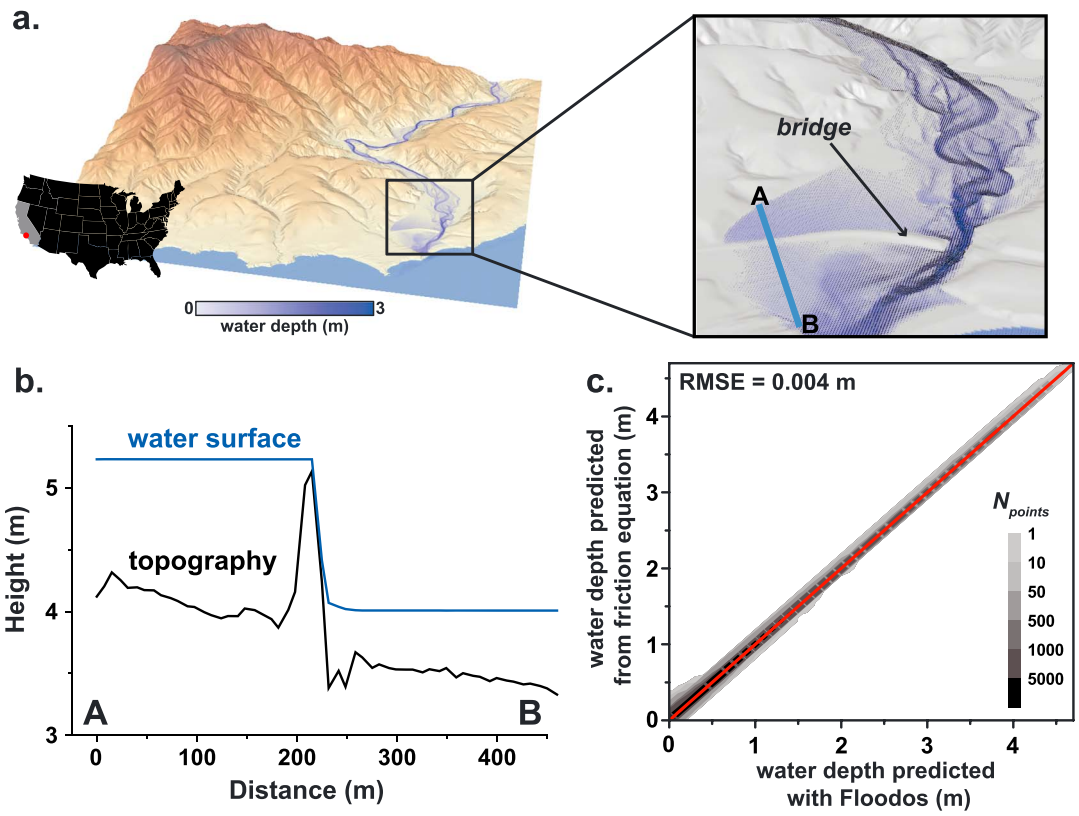

Figure 5. (a) Lidar DEM near Cruz Rock (USA) derived from airborne lidar data acquisition (Δx = 2.5 m) with a zoom of the floodplain area close to outlet. The blue scale colors represent the water depth; flow direction vectors weighted by discharge are shown in black. (b) Longitudinal profile through the downstream dam showing water surface on top of the topography. (c) Density plot of the water depth *h* calculated by *Floodos* (horizontal axis) versus *h* predicted from the Manning friction equation given discharge and water slope. The red line indicates a perfect agreement between both values.

We compare results obtained from *Floodos* with *Lisflood-FP*. The calculations were performed on both high- and low-resolution DEMs (2.5 m and 22.5 m, respectively) in order to appraise the grid resolution effects (Figure 7). Although *Lisflood-FP* underpredicts the water depth in a few places compared to what the friction equation would predict, both models give about consistent results for the 2.5 m grid (Figure 7a). For the low-resolution grid, *Lisflood-FP* systematically overpredicts water depth compared to *Floodos* (Figure 7b). With such a large resolution, a large part of the channels are made of one or two pixels, so that there are a large number of "wet" pixels that are surrounded by "dry" ones, as illustrated in Figure 7b (red areas). This is not a favorable configuration for the four-neighbor *Lisflood-FP* algorithm. On the contrary, *Floodos* uses an eight-neighbor algorithm and is insensitive to the wetting/drying issue. The results obtained from the low-resolution DEM are thus consistent with those from the high-resolution DEM (Figure 7c); the main discrepancies between both predictions reflect mostly pixels that are wet for the 2.5 m grid and dry pixels for 22.5 m grid.

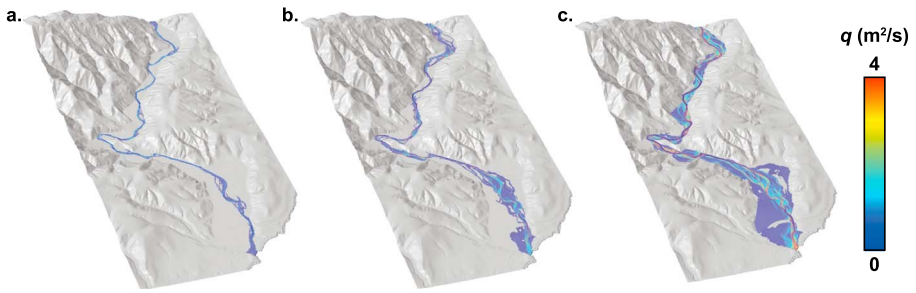

Figure 6. Picture of the predicted flood extent for different discharges in the Cruz DEM. (a) Q_{in} = 40 m^3 s^{-1}. (b) Q_{in} = 150 m^3 s^{-1}. (c) Q_{in} = 500 m^3 s^{-1}. *q* is the specific discharge.

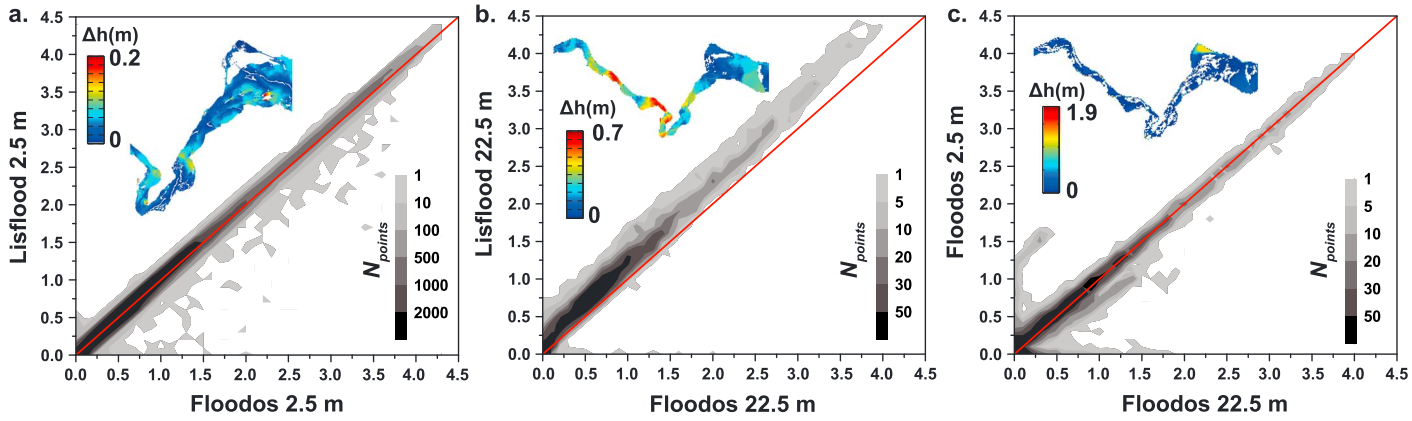

Figure 7. Density plot of the comparisons between *Floodos* and *Lisflood-FP* water depth predictions for different grid resolutions (red line is $h_{Floodos} = h_{Lisflood}$) along with a raster map of the difference of water depth predictions ((a) Δx = 2.5 m and (b) Δx = 22.5 m). (c) Density plot comparing *Floodos* water depth predictions for the same DEM with two resolutions of 2.5 m and 22.5 m, respectively.

4. Morphodynamic Modeling

The precipiton method was originally developed as a particle-based geomorphic model capable of resolving the stream power erosion equation, assuming that the hydraulic slope is similar to topographic slope and that the river width is a known function of flow (mainly discharge) and topographic parameters. In that respect, it is equivalent to most of the current landscape evolution models (see the review by *Tucker and Hancock* [2010]). It is also a reduced complexity model capable of mimicking the emerging properties of geomorphological systems such as braided patterns [*Castelltort et al.*, 2004; *Davy and Lague*, 2009]. The capacity of the precipiton method to resolve the shallow water equations, thus calculating hydraulic slopes, and to be easily coupled with erosion/deposition processes make it an efficient numerical method to explore complex river dynamics.

In the following, we will briefly describe the method and demonstrate its capacity to model the emergence of river width and braided patterns. These examples are presented as an illustration of the model ability to effectively couple hydrodynamic and erosion laws and to generate elementary fluvial instabilities.

4.1. Implementation of the Erosion Model

We use the implementation described in prior work [*Crave and Davy*, 2001; *Davy and Crave*, 2000; *Davy and Lague*, 2009], where each precipiton is eroding, transporting, and releasing sediments with given erosion and deposition laws. The erosion function $\dot{e}$ is controlled by the hydraulic shear stress τ and critical shear stress τ_c, where $\tau = \rho g h s$: $\dot{e} = k_e(\tau - \tau_c)^a$. Other erosion functions could have been used such as the stream-power law, which relates erosion to discharge q and hydraulic slope s [*Howard*, 1994; *Lague*, 2014; *Whipple and Tucker*, 1999]. Deposition rate $\dot{d}$ is proportional to the sediment flux q_s, $\dot{d} = \frac{q_s}{\xi}$, where ξ is a characteristic length, which controls the transport length of sediments and is assumed to be a function of discharge [*Davy and Lague*, 2009]. If ξ is much larger than flow distances, the system is detachment-limited, and is only controlled by local erosion rate $\dot{e}$; if ξ is small, the erosion/deposition equation is similar to a transport capacity equation where the sediment flux q_s is exactly equal to the product of the sediment transfer length ξ with local erosion rate $\dot{e}$: $q_s = \xi \dot{e}$.

Sediment fluxes in transverse direction to the main flow are also very important components in the geomorphodynamic process [*Schuurman et al.*, 2013]. Both lateral erosion ($\dot{e}_l$) and deposition (q_{sl}) fluxes are given by

$$\dot{e}_l = k_e \nabla_l H \, \dot{e} \tag{17}$$

$$q_{sl} = k_d \nabla_l H \, q_s \tag{18}$$

where $\nabla_l H$ is the topographic gradient orthogonal to the stream direction (referred to as the lateral topographic gradient) and k_e and k_d are the dimensionless coefficients for lateral erosion and lateral deposition, respectively. The main difference between equations (17) and (18) is that the former is expressed as the ratio of lateral versus basal erosion rates, while the latter is expressed as the ratio of lateral versus total, in stream, sediment flux.

The lateral erosion rate $\dot{e}_l$ models "bank-like" erosion processes. The lateral topographic gradient is also the geometrical ratio between basal and lateral surfaces, and the coefficient k_e reflects both changes in erodibility or erosion processes between basal and lateral erosion. Lateral erosion/deposition fluxes induce a transfer of matter between precipiton paths (i.e., flow streamlines) which is central to the emergence of channel forms.

The lateral deposition flux q_{sl} models lateral mass transfer due to either flow processes (transverse component of the bed shear stress induced by secondary flow) or gravity forces acting on the bed [*Ikeda*, 1982; *Ottevanger et al*., 2013; *Parker*, 1984]. The coefficient k_d reflects the efficiency of the lateral flow; it is likely dependent on the shear stress τ such as

$$k_d = \frac{1}{\alpha\sqrt{\theta}} \tag{19}$$

where θ is the Shields parameter, i.e., the shear stress normalized by the buoyant particle weight per unit area $\theta = \frac{\tau}{(\rho_s - \rho)gD}$, with ρ_s as the grain density, ρ as the water density, D as the average grain size, and α as a dimensionless parameter that varies between 0.35 and 1.5 [*Ikeda*, 1982; *Parker*, 1984; *Sekine and Parker*, 1992; *Talmon et al*., 1995]. The details of the equations, and of their implementation in the numerical code, are given in the supporting information.

4.2. Emergence of Straight Channels

As a basic test of the method, we simulate the emergence of a stream on a sloping plane. The model dimensions are 200 × 500 m and the initial slope is 1%. Water depths are computed according to the Manning equation with a friction coefficient of 0.025. Sediment fluxes are calculated by assuming that bed load transport dominates (i.e., the sediment transport distance ξ is small compared to system dimensions), and the sediment flux is given by the *Meyer-Peter and Muller* [1948] (MPM) equation $q_s = E(\tau - \tau_c)^a$, with $a = 1.5$, $E = 0.0002$ kg$^{-1.5}$ m$^{-3.5}$ s^{-2}, and $\tau_c = 4$ Pa (corresponding to a grain diameter of 8 mm). These conditions are obtained with $\xi = 2$ m, and the vertical erosion term $\dot{e} = \frac{q_s}{\xi} = \frac{E}{\xi}(\tau - \tau_c)^a$. An inflow is applied at the upstream boundary along a line of width 40 m, with a constant input discharge $Q = 15$ m^3 s^{-1}, and a fixed sediment volumetric concentration of 10%. The downstream conditions are described in the supporting information. The simulations have been computed in less than an hour on a standard PC.

The results of this experiment are given in Figure 8 with a grid size $\Delta x = 2$ m. The incision propagates downstream and forms a channel, whose slope is decreasing down to a stationary state where sediment inflow equal outflow. The channel width establishes rapidly in the upstream part of the model and slightly later downstream (Figure 8a). At the stationary stage, it is about constant all along the profile, except near the downstream boundary where the boundary conditions (no erosion and backwater effects) induce a widening of the channel, and near the inlet where the equilibrium channel is narrower than the width over which water is injected. The time evolution of the channel width is much faster than of channel slope and sediment flux (Figures 8b–8d).

Simulations have been performed with three different grid resolutions for different values of the lateral erosion parameter k_e (Figure 9). Although there exists a stochastic variability inherent to each simulation (precipitons are launched randomly at the upstream boundary), Figure 9 shows that the predicted channel geometries are largely independent of the grid size, which is a basic test to validate the numerical method that most of the reduced complexity models fail [*Doeschl-Wilson and Ashmore*, 2005; *Murray and Paola*, 1994; *Nicholas and Quine*, 2007; *Ziliani et al*., 2013]. We have also checked that the equilibrium channel width is independent of the water inlet width. The channel width depends mostly on both lateral erosion and deposition coefficient, k_e and k_d, respectively, defined in equations (17) and (18). With $k_d = 0.5$, simulations show that the channel width is independent of k_e if $k_e < 0.03$, and then increases proportional to $\log(k_e)$ if $k_e > 0.03$. The lower bound of simulated channel width is about 20 m, consistent with natural rivers with similar flow and sediment parameters (discharge of 15 m^3 s^{-1}, grain size of ~1 cm) [*Parker et al*., 2007].

4.3. Multithread Channels

We also reproduce the braided patterns that a previous version of €ros was already able to create with a simplified description of water surface hydraulics and lateral erosion [*Davy and Lague*, 2009]. Model and

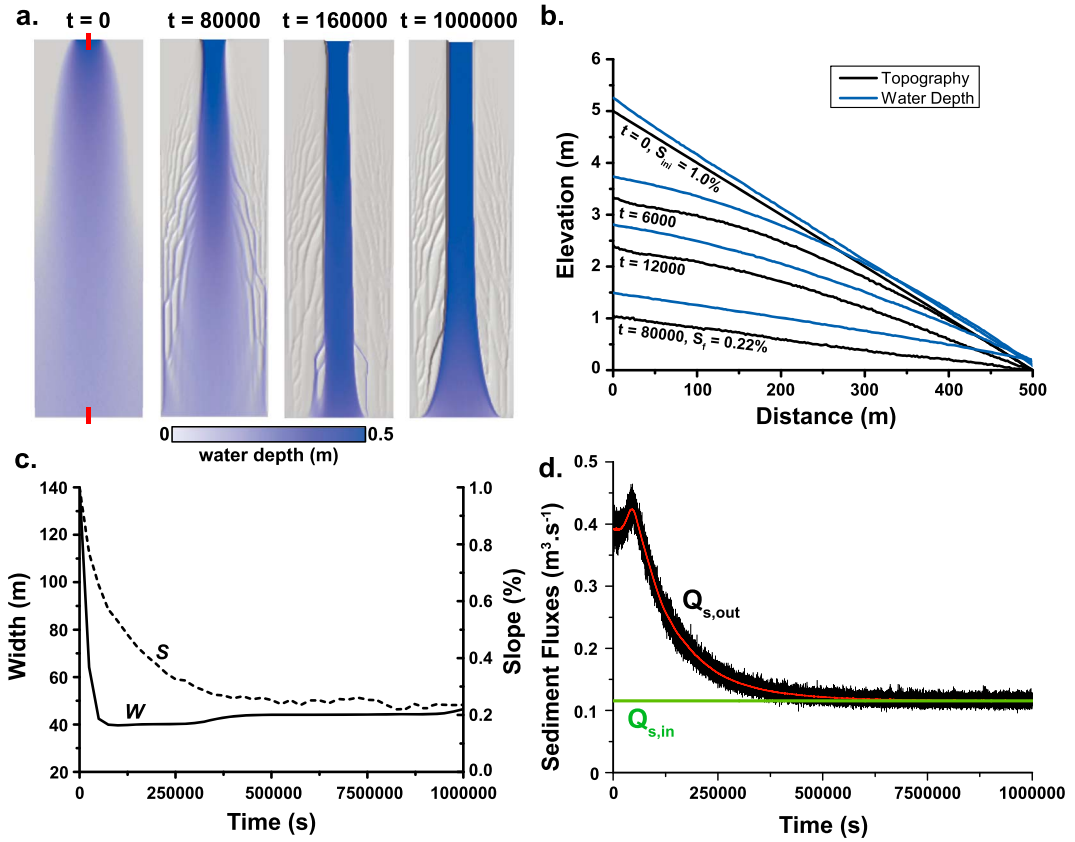

Figure 8. Simulation of the erosion of an initially flat sloping surface of 200 × 500 m with an initial slope of 1%, and a grid resolution $\Delta x = 2$ m. The upstream inflow Q is equal to 15 $m^3\ s^{-1}$. The erosion parameters are given in the text. (a) Snapshots of the temporal evolution of the formation single thread channel for the time steps 0, 6000, 12,000, and 80,000. (b) Elevation and water depth profile along the main channel at different time steps at x = 100 m (between the red lines). (c) Temporal evolution of channel width (black line, left vertical scale) and slope (dashed line, left vertical scale) measured at the center of the model. (d) Outflux as a function of time; the red curve is the average evolution obtained by filtering high-frequency variations.

boundary conditions are set to match roughly the Waimakariri River, New Zealand, which has been used as a field test for computing braided patterns by *Nicholas* [2000]. The initial topography is a planform of dimensions 800 × 5000 m with a grid resolution Δx = 10 m and an initial slope of 0.5%. The water depths are calculated assuming a Manning-type friction with $n = 0.035$. The entrainment of sediment is computed with a MPM equation and $\tau_c = 26.5$ Pa (average grain size of ~3 cm). Other parameters are a lateral deposition coefficient $k_d = 3^*\sqrt{\theta}$, lateral erosion parameters $k_e = 0.25$, and an upstream inflow $Q = 500\ m^3 s^{-1}$. The transport deposition length ξ was found to be a critical parameter for the development of braiding patterns [*Davy and Lague*, 2009], and we test both a value of the order of the grid size (experiment ξ20 with $\xi = 20$ m), and another one significantly larger (experiment ξ500, with $\xi = 500$ m). The simulations have been computed in about 50–70 h on a standard PC.

We let the system run with recirculating conditions; i.e., the total amount of outflowing sediment from the downstream boundary is reinjected into the upstream inlet boundary. This entails no variation of the mean topography, but a coupled evolution of sediment flux and channel geometry, which leads to the formation of braided patterns. The straight channel geometry described in the preceding section forms for initial conditions of net erosion (sediment influx much smaller than outflux during the initial transient stage), which emphasizes the important role of boundary conditions on the final geometry, the effects of which (e.g., sediment feed versus recirculation) are beyond the scope of this study.

Both simulations (with ξ=20 and 500 m, respectively) are characterized by an initial development stage preceding a stationary regime (at least in terms of sediment), which may slowly evolve on the long term. For ξ20,

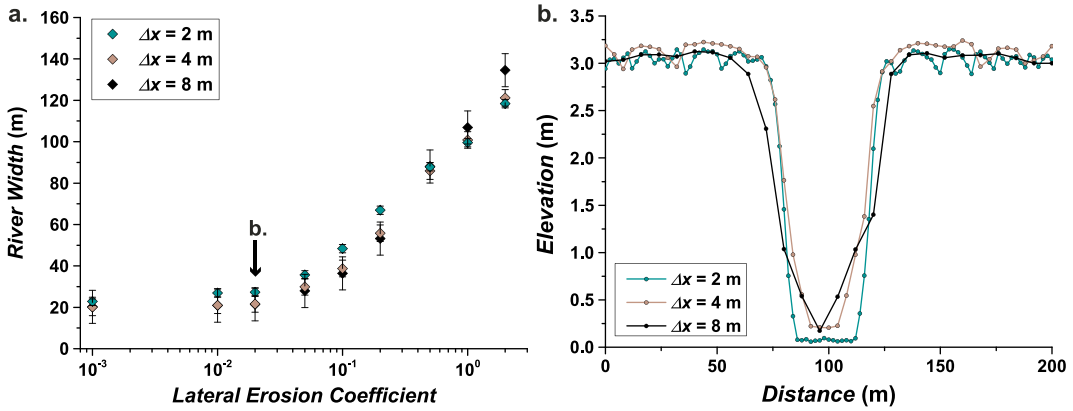

Figure 9. (a) River width at stationary stage for three different grid resolutions ($\Delta x = 2, 4, 8$ m) as a function of the lateral erosion parameter k_e defined in equation (17). (b) Channel cross section at the model center for $k_e = 2.10^{-2}$. All the other simulation parameters are described in the text.

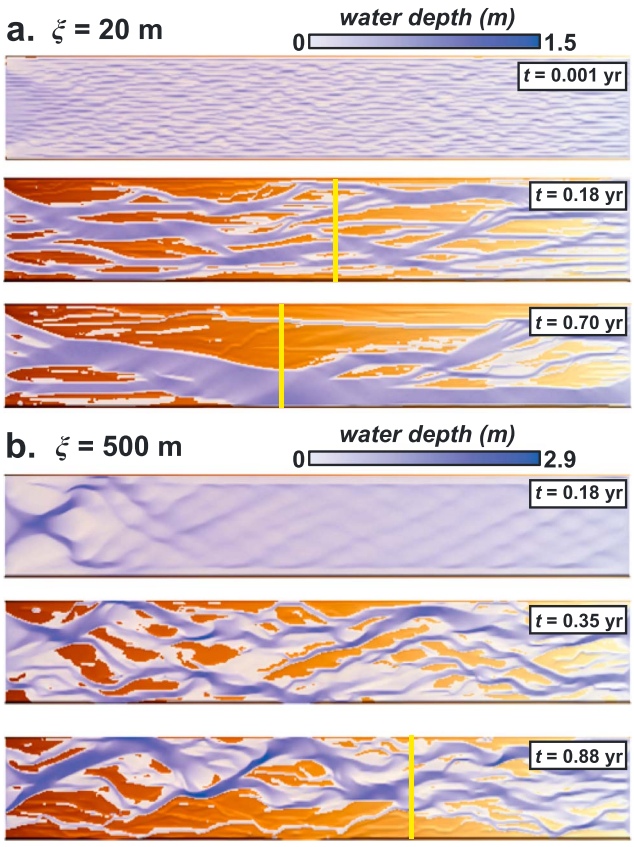

Figure 10. Top views of the channel patterns for both simulations described in the text with sediment recirculating conditions ((left) inlet and (right) outlet with constant topography). Simulations are performed with a deposition length of (a) 20 m and (b) 500 m. (second column) The time is given in years for a constant discharge of 400 m^3 s^{-1} (which would correspond to a much longer time in natural systems, considering the climate variability). The blue color scale is related to water depth, and the brown color corresponds to the locations with no flow. The yellow lines indicate the cross sections that are described in Figure 11.

the early stage is made of small-scale parallel microchannels spreading through the whole system (first plan view; Figure 10), and progressively merging to form larger channels. There is no limit to this process, and the system eventually organizes into a single channel; that is, no braiding instability is sustained over the long term. For ξ500, a rhomboidal instability initially forms (3-D plan view; Figure 10), whose spacing and angle depend on the lateral flux parameter of the deposition length ξ, and the lateral transfer coefficient k_d (this will be further developed in a subsequent paper). This is consistent with the results of *Devauchelle et al.* [2010], who proposed that the instability results from a coupling between flow and sediment transport rather than having a purely hydrodynamic origin. In which case, the braiding pattern develops by the degeneration of the regular initial instability into a single-thread alternate bar channel as previously observed by *Schuurman et al.* [2013] and, to a lesser extent, in *Nicholas et al.* [2013]. The braiding instability remains active throughout the experiment and, unlike the results for ξ20, the braids do not eventually collect into a single channel. Note that, although the "braiding instability" is initially shaped by the rhomboidal instability pattern, it is not clear whether both instabilities are physically linked.

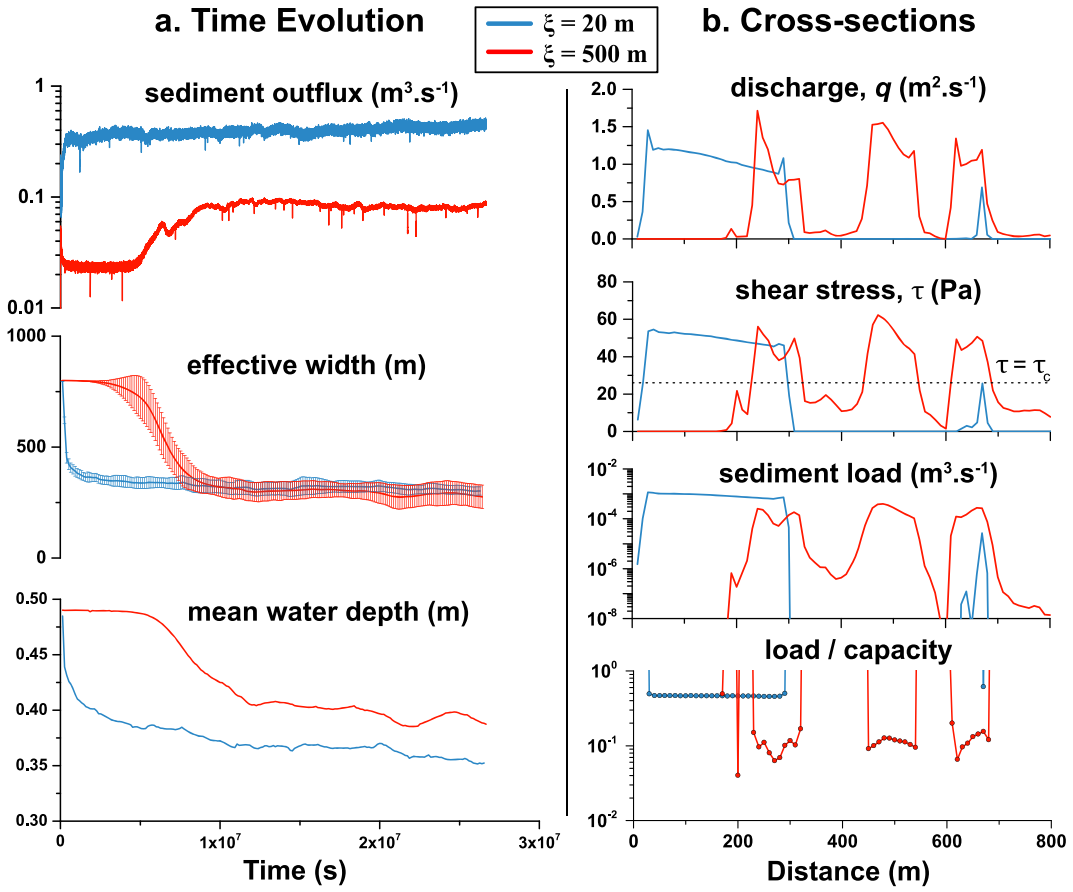

Figure 11. (a) History of the sediment flux, effective width (i.e., the width by discharge, calculated for each cross section perpendicular to flow $[0, L_y]$ as $W = \left(\int_0^{L_y} q(y)dy\right)^2 / \int_0^{L_y} q(y)^2 dy$, and averaged over all the cross sections except those affected by inlet and outlet boundary conditions), and mean water depth (average over all the "wet" pixels) for both multithread models. (b) Evolutions of the discharge per unit width q, stress τ, sediment load, and ratio of sediment load by stream capacity $\xi^* e$, for the two cross sections indicated in the last model stages of Figure 12 corresponding to $t = 0.7$ for $\xi 20$ (blue lines) and $t = 0.9$ for $\xi 500$ (red lines), respectively.

The specific recirculating boundary conditions maintain the topographic slope fixed on average, but neither the sediment flow nor the channel pattern is constrained, which allows the former to adapt to the latter and vice versa. The history of macroscopic parameters (sediment flux, effective width, mean water depth) are given in the Figure 11 (left column). Although very different in distribution, both models $\xi 20$ and $\xi 500$ converge to the same total effective width, which is roughly the sum of individual channel widths. The mean water depth is slightly higher in the $\xi 500$ than in the $\xi 20$ model, emphasizing a slightly larger dry surface in the latter. The models mainly differ by the total sediment flux that they can carry, which is 5 times larger in $\xi 20$ than in $\xi 500$ (Figure 11, top left), despite having identical asymptotic transport capacity laws.

This major difference between both models can be explained by a cross-section analysis of the channel characteristics (Figure 11, right column). For $\xi 20$ (red lines), the discharge is concentrated into one big channel, in which the shear stress is about 2 times the threshold, and the sediment load is half the total sediment capacity $q_s^{\infty} = \xi \dot{e}$. In addition to the main channel, there is a small braid, which carries sediment but is unable to erode. The rest of the model in this cross section is dry. The $\xi 500$ model at stage $t = 0.9$ is made of three main channels, all able to erode the channel bed with a shear stress about 2 times the threshold. The sediment load carried by the channels is only 10% of the potential capacity. A significant part of the cross section between channels is composed of flow that carries sediment without being able to erode (see the small channel at a distance of about 400 m; Figure 12, top cross section). In terms of downstream dynamics, net deposition can be observed in delta-like divergent structures with a downstream increase of the channel width that favors deposition fluxes compared to erosional ones. The depositional length ξ is a characteristic length of the

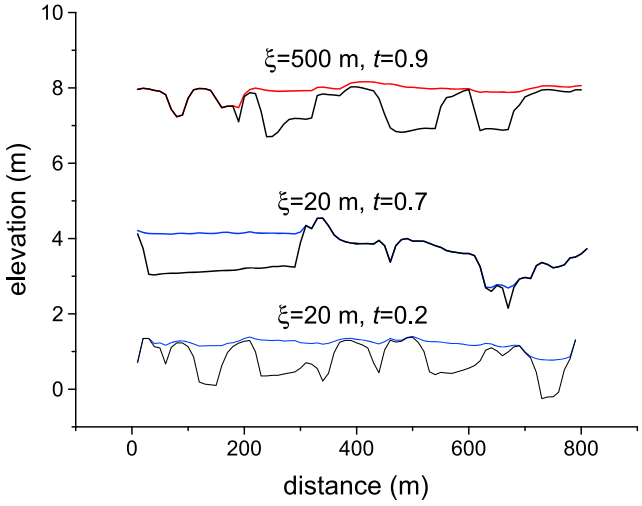

Figure 12. Three cross sections of both multithread simulations with topography (black line) and water surface (blue or red lines). The cross sections are indicated by the yellow lines in Figure 10.

channel pattern because it fixes the average distance between eroding and depositing zones and thus the average channel length. The interplay between eroding channels and deposition zones is basic to the braiding process.

5. Discussion

5.1. Potential and Limits of the Precipiton Method

The precipiton method was shown to be a versatile particle-based numerical method that differs from other numerical methods in several ways:

1. The approach is a Lagrangian method, and thus, it does not require an a priori delineation of the wetted area.
2. Particles are moving stochastically on a regular grid, which makes the approach easy to apply on DEMs.
3. The implementation of erosion/deposition rules in the Lagrangian framework is straightforward, as long as we consider no flow of sediment between water volumes.
4. Although the processes that are solved by the method are highly nonlinear, the precipitons can be processed one by one, independent of each other, in contrast with other particle-based methods such as smooth particle hydrodynamics.
5. The precipiton method effectively handles local minima (e.g., lakes).
6. The method also allows for a rapid calculation of the stationary solution. This is accomplished by the fact that the volume of water carried by the precipiton does not change along the downstream path. The water balance is not ensured for each precipiton but the stationary solution is theoretically correct. In these conditions, CPU time is roughly linear with the number of pixels N (Figure 13). Note that the method has not yet been parallelized, and we are currently developing a new version with precipitons managed in parallel.

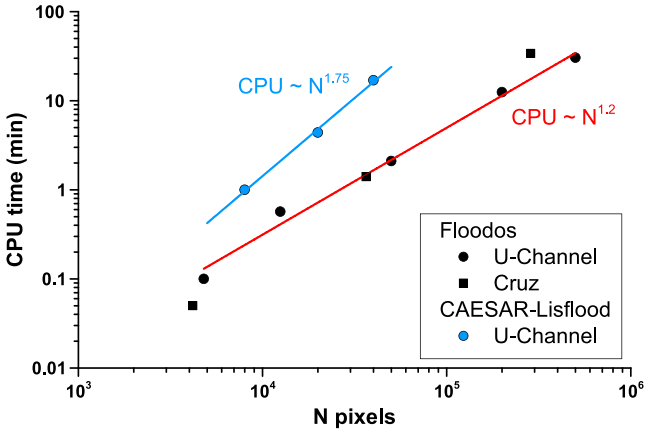

Figure 13. Computation time as a function of the number of wet pixels (Table 1) for the *U*-shaped channel (solid black circles) and Cruz case (solid black squares). For the *U*-shaped channel (see section 3.2), the computation time was recorded in the stationary regime. Calculations were performed using the largest time step value that respected the stability criteria defined in section 3.2. The computation time increased slightly nonlinearly with the number of pixels following a relationship: CPU time ~ $N^{1.2}$. The computation time followed a similar pattern for the real-case application ("Cruz," black square) described in section 3.4. For comparison, the results obtained with *Lisflood-FP* are indicated (blue dots). Although all the simulations are performed on the same computer, this test cannot be considered as a benchmark of both codes since *Lisflood-FP* calculates the transient regime, and it can certainly be better optimized if run by its developers.

The current limitations of the method are the following:

1. As is true for any explicit method, there is a lower limit of time increment for which an accurate solution may be obtained. In the precipiton method, the elementary water volume induces a roughness of the water surface,

which must remain smaller than the hydraulic gradients to ensure a correct prediction of the precipiton path.

2. The method solves the shallow water equations with no inertia terms such as advection and acceleration, meaning that the flow is assumed everywhere subcritical. This limitation is not intrinsic to the method. We are now working on improving the method by taking into account the inertia terms of equation (2) in the precipiton routing. We are also working on incorporating the vertical shear between water masses in the momentum equation (2).

The method is new and would require considerable additional work to make a comprehensive comparison of the advantages of the complete erosion/transport model with existing morphodynamic models such as H-STAR, CAESAR, DELFT 2D or 3D [*Coulthard et al*., 2013; *Lesser et al*., 2004; *Nicholas*, 2013b; *Schuurman et al*., 2013]. A key advantage of the model is the possibility to couple catchment-scale dynamics with river morphodynamics in order to explore hillslope-channel coupling and the understudied role of dynamic channel width on long-term landscape evolution. The high efficiency on a single CPU also enables the systematic exploration of a wide range of model parameters suitable for model inversion or ensemble simulations.

5.2. New Insights Into the Understanding of Geomorphic Instabilities

The ability of the precipiton model to efficiently couple hydrodynamics and erosion opens new possibilities to tackle problems as difficult as the emergence of geomorphic instabilities. After demonstrating that the method is able to generate simple channels, with a width independent of the resolution of the grid size, we simulated a braided pattern by applying recirculating conditions to a system of a given slope. Although the experiments are not comparable in terms of parameters and boundary conditions, the morphodynamic model is consistent with the results obtained by similar numerical codes that couple realistic hydrodynamics and sediment erosion/transfer equations [e.g., *Jang and Shimizu*, 2005; *Kleinhans*, 2010; *Nicholas*, 2013b; *Nicholas et al*., 2013; *Schuurman et al*., 2013; *Wang et al*., 2010], and our approach does not present the same limitations as the reduced complexity models [*Doeschl-Wilson and Ashmore*, 2005; *Murray and Paola*, 1997; *Murray and Paola*, 1994; *Thomas et al*., 2007]. The rhomboid instability in our braided simulations has been observed as an initial stage of several models [*Kleinhans*, 2010; *Nicholas et al*., 2013; *Schuurman et al*., 2013], as well as the widespread microchannel patterns observed in our experiment ξ20 [*Jang and Shimizu*, 2005].

A full analysis of the model and of the braiding instability is beyond the scope of this paper, but we emphasize several points that deserve further analysis.

1. The MPM equation that we use in our morphodynamic simulations predicts a small dependency of the flux with discharge ($q_s \sim q^{0.9}$if $\tau \gg \tau_c$ with both MPM and the Manning equation), in contrast with the *Engelund and Hansen* [1967] (EH) equation used in *Schuurman et al.* [2013], and in *Nicholas et al.* [2013] for sand transport rates, which predicts $q_s \sim q^{1.5}$. The only nonlinearity of our version of MPM is due both to the threshold stress τ_c, which entails large variations of q_s for shear stress close to τ_c, and to the deposition distance ξ, which yields highly nonlinear sediment flux ($q_s \sim q^{1.9}$ in our case) if the deposition flux is smaller than erosion rate (i.e., for distances smaller than ξ). Since the pioneering work of *Smith and Bretherton* [1972], it is known that the concentration of flow into channels is enhanced by a more-than-linear $q_s(q)$ relationship (i.e., $q_s \sim q^{\alpha}$ with $\alpha > 1$), which may enhance the braiding instability. The "less-than-linear" ($\alpha < 1$) ξ20 experiments show that the multithread pattern is a consequence of initial instabilities that tend to reduce over time by channel merging; this was also observed in *Jang and Shimizu* [2005], who used similar erosion laws (MPM with sediment at capacity). In contrast, the ξ500 experiment seems to illustrate a well-developed braiding pattern that differs significantly from the initial rhomboidal instability. This is observed in *Nicholas et al.* [2013] and *Schuurman et al.* [2013], who use the EH transport equation. Note that *Nicholas et al.* [2013] implicitly define a deposition length for the silt fraction, with a value on the order of 10 km as derived from their equation (23). *Schuurman et al.* [2013] assumed that sediment flux is at capacity for their standard model (they also run a model with the MPM equation, but gave no detail about it except the sediment outflux), but the absence of lateral erosion freezes the system in a shape very close to the initial rhomboidal instability. The issue of whether the instability is mainly driven by the nonlinearity of sediment flux versus discharge, by the deposition length as is the case for the development of sand ripples and dunes [*Andreotti et al*., 2002; *Charru et al*., 2013], or by secondary circulation due to turbulence (see the seminal works of *Parker* [1976], a feature that is not implemented in this model) is still an open question.

2. Both braiding experiments show that channels are not at capacity, with important consequences for the ability of the braided system to export large sediment fluxes. The deposition length ξ appears to be a primary control on braiding. Parameter ξ fixes the maximum distance for a system to be undercapacity and, because of this, controls the distance between erosional and depositional areas and thus the length of the braids. The necessary condition for ξ to control braid characteristics is that ξ is sufficiently large in natural systems, i.e., several times the channel width. Few attempts have been made to evaluate ξ for natural systems, but *Davy and Lague* [2009] show that, depending on grain size, ξ can be large enough to be a potential control on the braid patterns.
3. As already noticed by *Schuurman et al.* [2013], the lateral deposition flux (k_d coefficient) is critical for the development and shape of the braiding instability. Experiments with low k_d are not able to reproduce realistic braided patterns.
4. A difficulty when comparing models is that the applied boundary conditions may be a first-order control on the development of patterns. A net erosion system will lead to the development of a few well-incised channels with low lateral mobility, while an aggrading system will tend to develop deltas, which naturally tend to distribute sediments into different temporary channels due to a self-filling channel process. Varying the discharge and the sediment flux at the inlet boundary, as in other studies [*Kleinhans*, 2010; *Nicholas*, 2013a; *Nicholas et al*., 2013; *Schuurman et al*., 2013], may potentially control the erosion/deposition dynamics, reducing the role of autocyclic (internal) dynamics. The recirculating-sediment conditions that we use force the system to develop at a constant bulk slope, and thus to self-adapt both the sediment flux transported out of the system and the characteristics of the channel patterns. We believe that recirculating-sediment conditions are suitable for a benchmark comparison between models.

6. Conclusion

To our knowledge, this is the first attempt to use the precipiton method to calculate river water depth under the shallow water assumption. The method mimics the paths of water droplets from source to sink, and was initially designed to erode and transport matter along the path by transferring water and matter from cell to cell. The strength of the method developed by *Crave and Davy* [2001] is that the particles/precipitons are routed one by one on a regular grid, which makes the approach computationally fast. The flow is calculated from the recording of the times when the precipitons reach each cell, and the water depth is resolved along the flow path as a Lagrangian method.

Introducing the shallow water equations in the precipiton framework was carried out in two steps: (i) particles/precipitons move on top of the water surface, as is expected from the shallow water equations without the inertia terms, and (ii) the precipitons interact with the water surface to build up the water depth. For the latter step, each cell is filled up by precipitons when they flow into the cell, with precipitons subsequently leaking out at a rate which is given by the friction law. The water depth evolution is formally described by a stochastic differential equation that is solved each time a precipiton enters a cell. It produces stochastic values of the local water depth, whose average is the expected value. At each cell, the precipiton volume is updated to maintain the water balance.

We examine the hydraulic performance of the model for a variety of scenarios, showing good agreement with values predicted from Lisflood-FP for flood propagation in an idealized rectangular channel and for flood inundation of a natural river valley using high-resolution LiDAR topography. In addition, the precipiton method efficiently manages flow barriers and associated upstream lakes and reservoirs.

Coupling of the hydraulics with erosion/deposition equations as done in the €ros code is straightforward. In addition to defining the water depth, particles erode the river bed and banks, transport, and deposit sediments. A variety of erosion/transport equations can be implemented in this scheme including lateral erosion and lateral depositional fluxes. A few examples of channel formation have been presented to illustrate the method. In tests conducted here, the code shows no dependence of the final solution on grid size. The approach also successfully creates both straight and braided channels. The experiments shown in this paper demonstrate some interesting features regarding braiding instability that deserve further investigation, such as conditions for developing braiding patterns, the role of deposition length, the fact that channels are under capacity, and the role of lateral deposition fluxes.

Appendix A: Analysis of the Stochastic Equation

We demonstrate that the water depth solution of the stochastic equation (7) (or equation (12) in the case of constant slope s) gives the expected average as defined by equation (4), although it fluctuates with time as in Figure 1, if $\phi(h, s)$ depends only on h ($\phi(h, s)$ is denoted $\phi(h)$ hereafter). This encompasses the case where s is constant. Equation (9) can be integrated between two successive precipitons $p-1$ and p as

$$\Phi(h_p) = \Phi(h_{p-1}) + t_p - t_{p-1} \tag{A1}$$

with $\Phi(h) = \int \frac{\Delta x \Delta y}{\phi(h)} dh$. Equation (7) thus becomes

$$h_p = \Phi^{-1}\left(\Phi(h_{p-1}) + t_p - t_{p-1}\right) + \frac{V_p}{\Delta x \Delta y} \tag{A2}$$

If $t_p - t_{p-1} \ll \Phi(h_{p-1})$, the equation can be approximated by

$$h_p = h_{p-1} + \Phi^{-1'}\left(\Phi(h_{p-1})\right)\left(t_p - t_{p-1}\right) + \frac{V_p}{\Delta x \Delta y} \tag{A3}$$

where $\Phi^{-1'}$ is the derivative of Φ^{-1}. Eventually, we obtain

$$h_p = h_{p-1} - \frac{\phi(h_{p-1})}{\Delta x \Delta y}\left(t_p - t_{p-1}\right) + \frac{V_p}{\Delta x \Delta y} \tag{A4}$$

The time between two successive precipitons defines the flow discharge, as already mentioned by *Crave and Davy* [2001]: $\overline{t_p - t_{p-1}} = \frac{V_p}{Q}$. By calculating the average over p of the previous expression (with $\overline{h} = \langle h(t_p) \rangle = \langle h(t_{p-1}) \rangle$), we obtain

$$\phi(\overline{h}) = Q \tag{A5}$$

which demonstrates that the average water depth is that of the friction equation.

Acknowledgments

The authors are grateful to Tom Coulthard, Joe Wheaton, three anonymous reviewers, and the Editor for their comments that helped to improve the manuscript. We thank Edwin Baynes and John Selker for proofreading the manuscript. All data used in the simulations are reported in the manuscript. The code (executable) can be accessed at https://osur.univ-rennes1.fr/eros/. The source code can be obtained by making an inquiry to Philippe Davy (philippe.davy@univ-rennes1.fr).

References

Andreotti, B., P. Claudin, and S. Douady (2002), Selection of dune shapes and velocities—Part 1: Dynamics of sand, wind and barchans, *Eur. Phys. J. B*, *28*(3), 321–339.

Bates, P. D., and A. P. J. De Roo (2000), A simple raster-based model for flood inundation simulation, *J. Hydrol.*, *236*(1–2), 54–77, doi:10.1016/s0022-1694(00)00278-x.

Bates, P. D., M. S. Horritt, and T. J. Fewtrell (2010), A simple inertial formulation of the shallow water equations for efficient two-dimensional flood inundation modelling, *J. Hydrol.*, *387*(1–2), 33–45, doi:10.1016/j.jhydrol.2010.03.027.

Brackbill, J. U., D. B. Kothe, and H. M. Ruppel (1988), Flip: A low-dissipation, particle-in-cell method for fluid flow, *Comput. Phys. Commun.*, *48*(1), 25–38, doi:10.1016/0010-4655(88)90020-3.

Bradford, S. F., and B. F. Sanders (2002), Finite-volume model for shallow-water flooding of arbitrary topography, *J. Hydraul. Eng.*, *128*(3), 289–298.

Cao, Z. (2007), Comments on the paper by Guy Simpson and Sebastien Castelltort, "coupled model of surface water flow, sediment transport and morphological evolution," computers & geosciences 32 (2006) 1600–1614, *Comput. Geosci.*, *33*(7), 976–978, doi:10.1016/j.cageo.2006.11.009.

Castelltort, S., J. Van Den Driessche, and P. Davy (2004), Reply to comment on "How plausible are high-frequency sediment supply-driven cycles in the stratigraphic record?" by Jasper Knight, *Sediment. Geol.*, *164*(3–4), 331–334, doi:10.1016/j.sedgeo.2003.10.011.

Charru, F., B. Andreotti, and P. Claudin (2013), Sand ripples and dunes, *Annu. Rev. Fluid Mech.*, *45*, 469–493.

Chase, C. G. (1992), Fluvial landsculpting and the fractal dimension of topography, *Geomorphology*, *5*, 39–57.

Coulthard, T. J., and M. J. Van De Wiel (2006), A cellular model of river meandering, *Earth Surf. Processes Landforms*, *31*(1), 123–132.

Coulthard, T. J., J. C. Neal, P. D. Bates, J. Ramirez, G. A. M. de Almeida, and G. R. Hancock (2013), Integrating the LISFLOOD-FP 2D hydrodynamic model with the CAESAR model: Implications for modelling landscape evolution, *Earth Surf. Processes Landforms*, *38*(15), 1897–1906, doi:10.1002/esp.3478.

Crave, A., and P. Davy (2001), A stochastic "precipiton" model for simulating erosion/sedimentation dynamics, *Comput. Geosci.*, *27*(7), 815–827, doi:10.1016/S0098-3004(00)00167-9.

Davy, P., and A. Crave (2000), Upscaling local-scale transport processes in large-scale relief dynamics, *Phys. Chem. Earth Solid Earth Geod.*, *25*(6–7), 533–541, doi:10.1016/S1464-1895(00)00082-X.

Davy, P., and D. Lague (2009), Fluvial erosion/transport equation of landscape evolution models revisited, *J. Geophys. Res.*, *114*, F03007, doi:10.1029/2008JF001146.

de Almeida, G. A. M., and P. Bates (2013), Applicability of the local inertial approximation of the shallow water equations to flood modeling, *Water Resour. Res.*, *49*, 4833–4844, doi:10.1002/wrcr.20366.

De Boer, D. H. (2001), Self-organization in fluvial landscapes: Sediment dynamics as an emergent property, *Comput. Geosci.*, *27*(8), 995–1003, doi:10.1016/S0098-3004(00)00137-0.

Devauchelle, O., L. Malverti, É. Lajeunesse, C. Josserand, P. Y. Lagrée, and F. Métivier (2010), Rhomboid beach pattern: A laboratory investigation, *J. Geophys. Res.*, *115*, F02017, doi:10.1029/2009JF001471.

Doeschl-Wilson, A. B., and P. E. Ashmore (2005), Assessing a numerical cellular braided-stream model with a physical model, *Earth Surf. Process. Landf.*, *30*(5), 519–540, doi:10.1002/esp.1146.

Duvall, A., E. Kirby, and D. Burbank (2004), Tectonic and lithologic controls on bedrock channel profiles and processes in coastal California, *J. Geophys. Res.*, *109*, F03002, doi:10.1029/2003JF000086.
Engelund, F., and E. Hansen (1967), *A Monograph on Sediment Transport in Alluvial Streams*, p. 65, Teknisk forlag, Copenhagen.
Favis-Mortlock, D. (1998), A self-organizing dynamic systems approach to the simulation of rill initiation and development on hillslopes, *Comput. Geosci.*, *24*(4), 353–372, doi:10.1016/S0098-3004(97)00116-7.
Fonstad, M. A. (2006), Cellular automata as analysis and synthesis engines at the geomorphology-ecology interface, *Geomorphology*, *77*(3–4), 217–234.
Foufoula-Georgiou, E., V. Ganti, and W. E. Dietrich (2010), A nonlocal theory of sediment transport on hillslopes, *J. Geophys. Res.*, *115*, F00A16, doi:10.1029/2009JF001280.
Horritt, M. S., and P. D. Bates (2002), Evaluation of 1D and 2D numerical models for predicting river flood inundation, *J. Hydrol.*, *268*(1–4), 87–99, doi:10.1016/S0022-1694(02)00121-X.
Howard, A. D. (1994), A detachment-limited model of drainage basin evolution, *Water Resour. Res.*, *30*(7), 2261–2285, doi:10.1029/94WR00757.
Hunter, N. M., M. S. Horritt, P. D. Bates, M. D. Wilson, and M. G. F. Werner (2005), An adaptive time step solution for raster-based storage cell modelling of floodplain inundation, *Adv. Water Resour.*, *28*(9), 975–991, doi:10.1016/j.advwatres.2005.03.007.
Ikeda, S. (1982), Lateral bed load transport on side slopes, *J. Hydraul. Div. Am. Soc. Civ. Eng.*, *108*(11), 1369–1373.
Izumi, N., and G. Parker (1995), Inception of channelization and drainage basin formation: Upstream-driven theory, *J. Fluid Mech.*, *283*, 341–363, doi:10.1017/S0022112095002357.
Jang, C.-L., and Y. Shimizu (2005), Numerical simulation of relatively wide, shallow channels with erodible banks, *J. Hydraul. Eng.*, *131*(7), 565–575.
Kleinhans, M. G. (2010), Sorting out river channel patterns, *Prog. Phys. Geogr.*, *34*(3), 287–326, doi:10.1177/0309133310365300.
Lague, D. (2010), Reduction of long-term bedrock incision efficiency by short-term alluvial cover intermittency, *J. Geophys. Res.*, *115*, F02011, doi:10.1029/2008JF001210.
Lague, D. (2014), The stream power river incision model: Evidence, theory and beyond, *Earth Surf. Processes Landforms*, *39*(1), 38–61, doi:10.1002/esp.3462.
Lave, J., and J. P. Avouac (2001), Fluvial incision and tectonic uplift across the Himalayas of central Nepal, *J. Geophys. Res.*, *106*(B11), 26561–26591.
Lee, H., and S. Han (2010), Solving the shallow water equations using 2D SPH particles for interactive applications, *Vis. Comput.*, *26*(6–8), 865–872.
Lesser, G. R., J. A. Roelvink, J. A. T. M. van Kester, and G. S. Stelling (2004), Development and validation of a three-dimensional morphological model, *Coast. Eng.*, *51*(8–9), 883–915, doi:10.1016/j.coastaleng.2004.07.014.
Li, S., and W. K. Liu (2002), Meshfree and particle methods and their applications, *Appl. Mech. Rev.*, *55*(1), 1–34, doi:10.1115/1.1431547.
Liu, G.-R., and M. Liu (2003), *Smoothed Particle Hydrodynamics: A Meshfree Particle Method*, 405 pp., World Sci. Co. Pte. Ltd., Singapore.
Manning, R. (1891), On the flow of water in open channels and pipes, *Trans. Inst. Civil Eng. Ireland*, *20*, 161–207.
Martz, L. W., and J. Garbrecht (1998), The treatment of flat areas and depressions in automated drainage analysis of raster digital elevation models, *Hydrol. Process.*, *12*(6), 843–855, doi:10.1002/(SICI)1099-1085(199805)12:6<843::AID-HYP658>3.0.CO;2-R.
Meyer-Peter, E., and R. Muller (1948), Formulas for bedload transport, in *Proceedings of the 2nd Meeting of the International Association for Hydraulic Structures Research*, pp. 39–64, Int. Assoc. for Hydraulic Structur. Res., Stockholm.
Murray, A., and C. Paola (1997), Properties of a cellular braided-stream model, *Earth Surf. Processes Landforms*, *22*, 1001–1025.
Murray, A. B., and C. Paola (1994), A cellular model of braided rivers, *Nature*, *371*, 54–57.
Nicholas, A. (2013a), Morphodynamic diversity of the world's largest rivers, *Geology*, *41*(4), 475–478, doi:10.1130/g34016.1.
Nicholas, A. P. (2013b), Modelling the continuum of river channel patterns, *Earth Surf. Processes Landforms*, *38*(10), 1187–1196, doi:10.1002/esp.3431.
Nicholas, A. P. (2000), Modelling bedload yield in braided gravel bed rivers, *Geomorphology*, *36*(1–2), 89–106, doi:10.1016/S0169-555X(00)00050-7.
Nicholas, A. P. (2005), Cellular modelling in fluvial geomorphology, *Earth Surf. Processes Landforms*, *30*(5), 645–649.
Nicholas, A. P., and T. A. Quine (2007), Crossing the divide: Representation of channels and processes in reduced-complexity river models at reach and landscape scales, *Geomorphology*, *90*(3–4), 318–339, doi:10.1016/j.geomorph.2006.10.026.
Nicholas, A. P., P. J. Ashworth, G. H. Sambrook Smith, and S. D. Sandbach (2013), Numerical simulation of bar and island morphodynamics in anabranching megarivers, *J. Geophys. Res. Earth Surf.*, *118*, 2019–2044, doi:10.1002/jgrf.20132.
Ottevanger, W., K. Blanckaert, W. S. J. Uijttewaal, and H. J. de Vriend (2013), Meander dynamics: A reduced-order nonlinear model without curvature restrictions for flow and bed morphology, *J. Geophys. Res. Earth Surf.*, *118*, 1118–1131, doi:10.1002/jgrf.20080.
Parker, G. (1976), On the cause and characteristic scales of meandering and braiding in rivers, *J. Fluid Mech.*, *76*(3), 457–480, doi:10.1017/S0022112076000748.
Parker, G. (1984), Discussion of "lateral bed load transport on side slopes" by Syunsuke Ikeda (November, 1982), *J. Hydraul. Eng.*, *110*(2), 197–199, doi:10.1061/(ASCE)0733-9429(1984)110:2(197).
Parker, G., P. R. Wilcock, C. Paola, W. E. Dietrich, and J. Pitlick (2007), Physical basis for quasi-universal relations describing bankfull hydraulic geometry of single-thread gravel bed rivers, *J. Geophys. Res.*, *112*, F04005, doi:10.1029/2006JF000549.
Ruther, N., and N. R. B. Olsen (2007), Modelling free-forming meander evolution in a laboratory channel using three-dimensional computational fluid dynamics, *Geomorphology*, *89*(3–4), 308–319.
Schuurman, F., W. A. Marra, and M. G. Kleinhans (2013), Physics-based modeling of large braided sand-bed rivers: Bar pattern formation, dynamics, and sensitivity, *J. Geophys. Res. Earth Surf.*, *118*, 2509–2527, doi:10.1002/2013JF002896.
Sekine, M., and G. Parker (1992), Bed-load transport on transverse slope. I, *J. Hydraul. Eng.*, *118*, 513–535.
Simon, A., and C. R. Thorne (1996), Channel adjustment of an unstable coarse-grained stream: Opposing trends of boundary and critical shear stress, and the applicability of extremal hypotheses, *Earth Surf. Processes Landforms*, *21*(2), 155–180.
Smith, T. R., and F. P. Bretherton (1972), Stability and the conservation of mass in drainage basin evolution, *Water Resour. Res.*, *8*(6), 1506–1529, doi:10.1029/WR008i006p01506.
Solenthaler, B., P. Bucher, N. Chentanez, M. Müller, and M. Gross (2011), SPH Based Shallow Water Simulation, paper presented at Eight Workshop on Virtual Reality Interactions and Physical Simulation, The Eurographics Assoc., Lyon.
Stark, C. P., E. Foufoula-Georgiou, and V. Ganti (2009), A nonlocal theory of sediment buffering and bedrock channel evolution, *J. Geophys. Res.*, *114*, F01029, doi:10.1029/2008JF000981.
Talmon, A. M., N. Struiksma, and M. C. L. M. Van Mierlo (1995), Laboratory measurements of the direction of sediment transport on transverse alluvial-bed slopes, *J. Hydraul. Res.*, *33*(4), 495–517, doi:10.1080/00221689509498657.

Tarboton, D. G. (1997), A new method for the determination of flow directions and upslope areas in grid digital elevation models, *Water Resour. Res.*, *33*(2), 309–319, doi:10.1029/96WR03137.

Tetzlaff, D. M., and J. W. Harbaugh (1989), *Simulating Clastic Sedimentation*, 202 pp., Van Nostrand Reinhold, New York.

Thomas, R., and A. P. Nicholas (2002), Simulation of braided river flow using a new cellular routing scheme, *Geomorphology*, *43*(3–4), 179–195.

Thomas, R., A. P. Nicholas, and T. A. Quine (2007), Cellular modelling as a tool for interpreting historic braided river evolution, *Geomorphology*, *90*(3–4), 302–317.

Tucker, G. E., and G. R. Hancock (2010), Modelling landscape evolution, *Earth Surf. Processes Landforms*, *35*(1), 28–50.

Turcotte, R., J. P. Fortin, A. N. Rousseau, S. Massicotte, and J. P. Villeneuve (2001), Determination of the drainage structure of a watershed using a digital elevation model and a digital river and lake network, *J. Hydrol.*, *240*(3–4), 225–242, doi:10.1016/S0022-1694(00)00342-5.

Wang, H., G. Zhou, and X. Shao (2010), Numerical simulation of channel pattern changes part II: Application in a conceptual channel, *Int. J. Sed. Res.*, *25*(4), 380–390, doi:10.1016/S1001-6279(11)60005-X.

Whipple, K. X., and G. E. Tucker (1999), Dynamics of the stream-power river incision model: Implications for height limits of mountain ranges, landscape response timescales, and research needs, *J. Geophys. Res.*, *104*(B8), 17661–17674.

Whittaker, A. C., P. A. Cowie, M. Attal, G. E. Tucker, and G. P. Roberts (2007), Bedrock channel adjustment to tectonic forcing: Implications for predicting river incision rates, *Geology*, *35*(2), 103–106.

Zhu, D., Q. Ren, Y. Xuan, Y. Chen, and I. D. Cluckie (2013), An effective depression filling algorithm for DEM-based 2-D surface flow modelling, *Hydrol. Earth Syst. Sci.*, *17*(2), 495–505, doi:10.5194/hess-17-495-2013.

Ziliani, L., N. Surian, T. J. Coulthard, and S. Tarantola (2013), Reduced-complexity modeling of braided rivers: Assessing model performance by sensitivity analysis, calibration, and validation, *J. Geophys. Res. Earth Surf.*, *118*, 2243–2262, doi:10.1002/jgrf.20154.